Research Article | Vol. 11, No. 2 / 1 February 2021 / Optical Materials Express 559
Optical Materials EXPRESS

Direct observation of modal hybridization in nanofluidic fiber [Invited]

André D. Gomes,[1,2] Jiangbo Tim Zhao,[1] Alessandro Tuniz,[3,4] and Markus A. Schmidt[1,5,6,*]

[1]Leibniz Institute of Photonic Technology, 07745 Jena, Germany
[2]Centre for Applied Photonics, INESC TEC, and Department of Physics and Astronomy, Faculty of Sciences, University of Porto, 4169-007 Porto, Portugal
[3]Institute of Photonics and Optical Science (IPOS), School of Physics, The University of Sydney, NSW 2006, Australia
[4]The University of Sydney Nano Institute (Sydney Nano), The University of Sydney, NSW 2006, Australia
[5]Otto Schott Institute of Materials Research (OSIM), Friedrich Schiller University of Jena, 07743 Jena, Germany
[6]Abbe Center of Photonics and Faculty of Physics, Friedrich-Schiller-University Jena, 07743 Jena, Germany
*markus.schmidt@leibniz-ipht.de

Abstract: Hybrid-material optical fibers enhance the capabilities of fiber-optics technologies, extending current functionalities to several emerging application areas. Such platforms rely on the integration of novel materials into the fiber core or cladding, thereby supporting hybrid modes with new characteristics. Here we present experiments that reveal hybrid mode interactions within a doped-core silica fiber containing a central high-index nanofluidic channel. Compared with a standard liquid-filled capillary, calculations predict modes with unique properties emerging as a result of the doped core/cladding interface, possessing a high power fraction inside and outside the nanofluidic channel. Our experiments directly reveal the beating pattern in the fluorescent liquid resulting from the excitation of the first two linearly polarized hybrid modes in this system, being in excellent agreement with theoretical predictions. The efficient excitation and beat of such modes in such an off-resonance situation distinguishes our device from regular directional mode couplers and can benefit applications that demand strong coupling between fundamental- and higher-order- modes, e.g. intermodal third-harmonic generation, bidirectional coupling, and nanofluidic sensing.

1. Introduction

Optical fibers represent one of the most successful devices in photonics, having revolutionized a number of fields such as telecommunications, nonlinear frequency conversion, and bioanalytics [1–3]. The transverse light confinement in commonly used cylindrical step index fibers is provided by a larger refractive index in the core than in the cladding leading to the formation of guided modes in the central core region. Depending on material distribution and geometric parameters, higher-order modes (HOMs) with distinct intensity and polarization patterns that cut-off under certain condition can form in addition to the Gaussian-like fundamental mode [4]. One benchmark figure that characterizes these modes is the waveguide V-parameter, which in the case of a cylindrical geometry is defined by $V = 2\pi a k_0 \sqrt{n_1^2 - n_2^2}$ (core radius: a; vacuum wave vector: $k_0 = 2\pi/\lambda$; vacuum wavelength: λ; refractive index of core and cladding: n_1 and n_2). The most successful material platform that is currently being used in the context of step index fibers is silica glass, where dopants such as germanium (GeO_2), alumina (Al_2O_3), phosphorus pentoxide (P_2O_5), or fluorine are used to increase or reduce the refractive index of silica [5–8]. In particular, cores composed of GeO_2-doped silica are globally employed as

#413199 https://doi.org/10.1364/OME.413199
Journal © 2021 Received 21 Oct 2020; revised 15 Dec 2020; accepted 23 Dec 2020; published 28 Jan 2021

Optical Materials EXPRESS

step-index fibers with wide transparency windows in the visible and near infrared spectral domain. In spite of its great success, doped silica step-index fibers with one material interface show limited capabilities for modal engineering due to the small number of parameters that can actually be varied. Increasing the accessible parameters space is crucial in applications that demand precise modal engineering, such as phase-matching, ultra-fast nonlinear frequency conversion, or mode coupling, all of which clearly benefit from fibers with extended modal tuning opportunities. One approach to increase the flexibility of optical fibers is the integration of novel materials, leading to so-called hybrid optical fibers (HOFs) [9]. During that last decade, a great variety of materials including metals [10,11], semiconductors [12–14] and high index glasses such as chalcogenides [15,16] have been incorporated into fiber for applications in a multitude of fields including plasmonics [17], optoelectronics [18] or nonlinear frequency conversion [19,20]. A novel class of HOFs that has recently emerged relies on the inclusion of liquids in silica fiber or capillary. Compared to fibers containing only solid materials, liquid-based HOF implementation is considerably more straightforward, since it relies on liquid infiltration of fiber nanochannels via capillary action. This type of HOF is a particularly attractive in terms of tunability, since liquids can be exchanged in real-time, and because their thermo-optic coefficients can reach those of semiconductor materials (e.g., CS_2: $\partial n/\partial T \approx 8 \times 10^{-4} K^{-1}$) [21]. Due to these unique properties, liquid HOFs have opened up new areas of applications in fiber optics, including micro- and nano-object detection [22–24], refractive index sensing [25–29], lab-on-a-fiber technology [30], chemistry [31,32], nonlinear optics [33–37], optoelectronics and lasing [38,39], as well as the observation of new physics (e.g., hybrid solitons [40]). The inclusion of novel materials, and liquids in particular, therefore greatly enhances and extends the capabilities of optical fibers to fields that would otherwise be challenging to address.

Here we experimentally demonstrate that the inclusion of a high refractive index nanofluidic channel in the center of a doped silica fibers leads to a novel type of a HOF supporting hybrid modes that have different modal properties than the modes of regular step index fibers (Fig. 1(a)). Simulations indicate a characteristic mode hybridization, which leads to mode formation that only emerge due to the presence of the additional material interface. The mode hybridization in this off-resonance situation is confirmed via mode-coupling experiments, whereby the fluorescently emitted and microscopically detected light reveals a spatially alternating intensity distribution due to the interference between the modes supported.

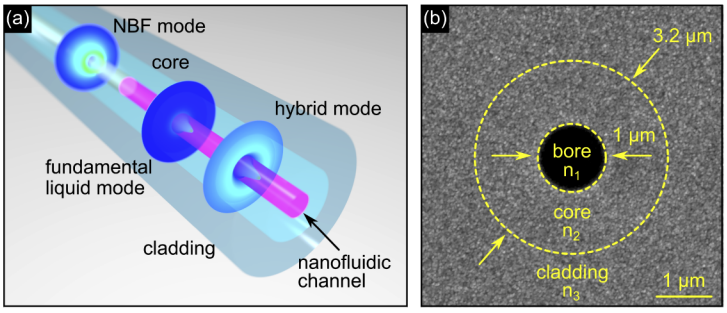

Fig. 1. (a) Schematic diagram of the hybrid optical fiber, relevant modes, and experimental concept: the fundamental NBF mode excites the two hybrid modes in the nanofluidic channel region, resulting in periodic power exchange between the silica and liquid. (b) Scanning electron microscope image of the central region of the fiber andrelevant parameters as labelled.

Optical Materials EXPRESS

2. Device Analysis

The HOF considered here consists of a step-index fiber geometry with silica cladding (outer diameter 180 μm, refractive index n_3 [41] and a GeO_2-doped core region (diameter d_c = 3.2 μm, doping level 11 mol%, refractive index $n_2 = n_3 + 8 \times 10{-}3$) that includes a central nano-channel (diameter d_b = 1.0 μm, refractive index n_1) that can be either air or a liquid. An illustration of the HOF and a scanning electron microscope (SEM) image of the central region of the nanobore fiber (NBF) are shown in Fig. 1(a) and (b), respectively. The fundamental condition to obtain the modal hybridization targeted here is the use of a refractive index inside the nano-channel that is higher than that of the surrounding core ($n_1 > n_2$) preventing the formation of evanescent fields inside the liquid. Based on a preliminary analysis, we choose a liquid bore material consisting of a solution of 0.45 molar fraction of ethanol (C_2H_5OH) in benzyl alcohol (C_7H_8O), which can be integrated into the fiber via capillary action. Using a one-resonance Sellmeier fit, the refractive index of the solvent mixture at 20° is given by

$$n_1^2(\lambda) = 1 + \frac{1.15201\lambda^2}{\lambda^2 - 0.016166}, \tag{1}$$

where the wavelength λ is expressed in μm.

In order to reveal the properties of the modal hybridization, the effective indices of the relevant modes n_{eff} have been calculated as a function of the relative refractive index of core and cladding $\Delta n = n_2 - n_3$ at a constant wavelength (λ = 532 nm, Figs. 2(a) and (b)), using Finite Element modeling and a semi-analytic approach [42]. Note that the situation $\Delta n = 0$ corresponds to a step-index fiber with a liquid core and a homogeneous silica cladding, which supports a single mode since $V = 1.75 < 2.401$. Increasing the core index imposes a second dielectric interface into the system, leading to the appearance of higher-order modes with distinct intensity patterns in the doped region. In the case discussed here, three higher-order modes emerge at $\Delta n = 4.2 \times 10{-}3$, which resemble the characteristic polarization patterns of the first set of HOMs from a regular step index fiber [42] (Fig. 2(f)-(h)). At $\Delta n = 5.9 \times 10{-}3$ the formation of another mode with a HE_{12}-like intensity and polarization pattern is observed (Fig. 2(e)). This mode is particularly interesting since it shows a linear polarization and a Gaussian-type intensity distribution, comparable to that of the fundamental mode in the central liquid region (2(d)). As a result, in the subsequent analysis we focus on the interference of the HE_{11} and HE_{12} modes, which will be experimentally revealed by microscopically monitoring the side-wise emitted fluorescent light. Note that for a decreasing bore diameter, the beat length increases up to a maximum of 56.3 μm at a bore diameter of 756 nm. For smaller bore diameters, the HE_{12} mode cuts off and the fiber supports only one linearly polarized mode.

One main difference between the modes of the nanofluidic channel enhanced fiber and a regular step-index fiber is the transverse power distribution in the different materials and the related mode field diameter (MFD), which is revealed here by simulating the fraction of power inside the liquid $f_{liquid} = \int_{A_{\text{bore}}} S_z dA / \int_{A_\infty} S_z dA$ (S_z: longitudinal Poynting vector) (Fig. 2(c)): In the nanofluidic channel enhanced fiber, the fundamental liquid mode (HE_{11}-mode, Fig. 2(d)) has a MFD that is determined by the size of the liquid filled bore, leading to about half of the electromagnetic power being localized inside the liquid (f_{liquid} = 0.5, green curve in Fig. 2(c)). For the TE_{01}, TM_{01}, HE_{21} and HE_{12} modes (Fig. 2(e)-(h)), however, the mode diameter is significantly larger and is determined by the size of the doped glass region. As a consequence the mentioned modes show a significantly smaller fraction of power inside the liquid ($f_{liquid} \leq 0.1$, Fig. 2(c)) compared to a liquid core fiber that has no second glass interface.

Following an earlier approach that can be applied to any kind of dual-waveguide coupler [43], the beating between the two modes leads to a well-known periodic intensity distribution along the z-direction. The distribution of the power in the liquid bore is determined as follows. The first step involves the calculation of the electric and magnetic fields (**E** and **H**) of the two

Optical Materials EXPRESS

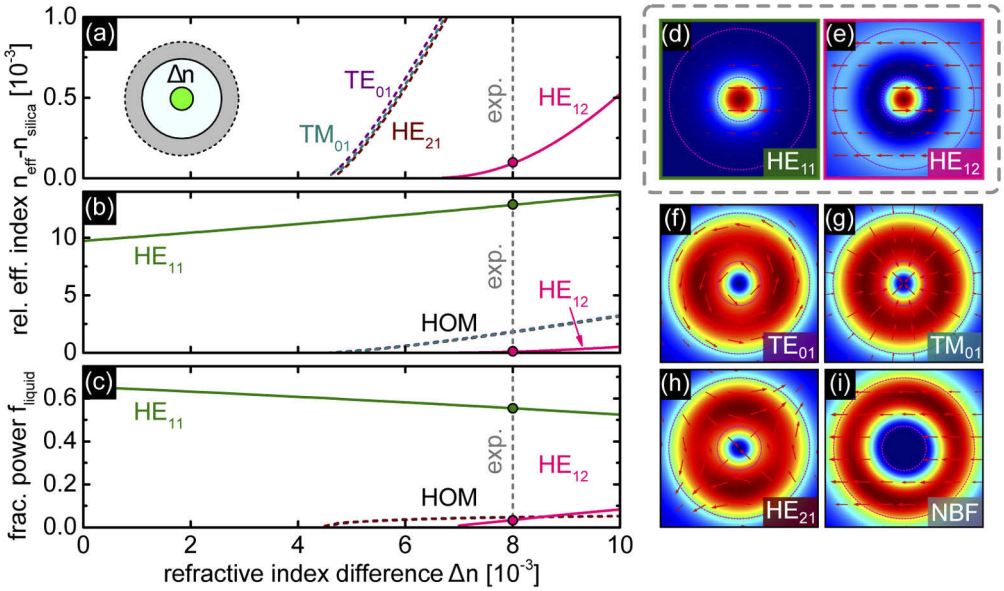

Fig. 2. Modal properties of the hybrid fiber. (a) Effective index (relative to the index of silica) of the relevant modes as function of refractive index difference of the core relative to the cladding Δn. The plot shown in (b) displays a larger spectral range in order to show the properties of the HE_{11}-mode. (c) Corresponding fraction of power inside the liquid. The images on the right show the Poynting vector distributions of the modes discussed at $\Delta n = 8 \times 10{-}3$ which corresponds to the experimentally investigated configuration ((d) HE_{11}, (e) HE_{12}, (f) TE_{01}, (g) TM_{01}, (h) HE_{21}). The HE_{11}- and HE_{12}- modes ((d) and (e)) that are addressed in the mode beating experiments are highlighted by the dashed gray frame. The pattern shown in (i) refers to the fundamental mode of the empty nanobore fiber. All calculations are conducted at a wavelength of $\lambda = 532$ nm.

relevant Eigenmodes in the liquid-filled fiber section ($\mathbf{E}_{HE_{11}}$=$\mathbf{E}_1$ and $\mathbf{E}_{HE_{12}}$=$\mathbf{E}_2$), as well as those the fundamental mode of the empty nanobore fiber ($\mathbf{E}_{NBF}$=$\mathbf{E}_3$, Fig. 2(g)). The latter represents the incoming mode (i.e, the mode that is launched at the fiber input) exciting the two hybrid Eigenmodes in the liquid-filled section. At the beginning of the coupling (i.e., liquid) section, the fraction of modal power transferred to each of the two Eigenmodes is calculated via the overlap integral

$$f_i = \frac{1}{N_i N_3}\left[\int_{A_\infty} (\mathbf{E}_i(x,y) \times \mathbf{H}_3(x,y))_z \, dA\right]^2 \tag{2}$$

where A_∞ is the entire cross section, and $N_i = \frac{1}{2}|\int_{A_\infty} \mathbf{E}_i \times \mathbf{H}_i dA|$ are the modal normalization constants ($i = 1, 2, 3$ as defined above, x and y: transverse coordinates). For the parameters considered here $f_1 = 0.17$ and $f_2 = 0.54$ showing that the HE_{12} mode is more efficiently excited, due to its larger overlap with the fundamental mode of the empty nanobore fiber (Fig. 2(i)). Note that the fundamental mode of the empty nanobore fiber is linearly polarized and has an annulus-type intensity distribution due to the evanescent decay of the fields towards the center of the channel overall resulting from the low refractive index of the air bore. Since the beating between the modes is experimentally confirmed on the basis of side-wise detection of fluorescent light, it is important to analyze the longitudinal power distribution inside the liquid region. To calculate this, we consider the transverse electric- and magnetic- fields as a function of the longitudinal coordinate z,

$$\mathbf{E}(x,y,z) = \sqrt{f_1}\mathbf{E}_1(x,y)\exp(ik_0 n_{\text{eff},1} z) + \sqrt{f_2}\mathbf{E}_2(x,y)\exp(ik_0 n_{\text{eff},2} z), \tag{3}$$

Optical Materials EXPRESS

$$\mathbf{H}(x,y,z) = \sqrt{f_1}\mathbf{H}_1(x,y)\exp(ik_0 n_{\text{eff},1}z) + \sqrt{f_2}\mathbf{H}_2(x,y)\exp(ik_0 n_{\text{eff},2}z). \quad (4)$$

with the effective indices of the HE_{11}- and HE_{12}-modes $n_{\text{eff},1}$ and $n_{\text{eff},2}$, respectively. At each z, the Poynting vector $S_z(x,y,z) = \frac{1}{2}\text{Re}(\mathbf{E}(\text{x, y, z}) \times \mathbf{H}^*(\text{x, y, z}))_\text{z}$ has been determined, which in the present case is given by

$$S_z(x,y) = \frac{1}{2}\left[f_1 q_1(x,y) + f_2 q_2(x,y) + \sqrt{f_1 f_2}\, q_{12}(x,y)\cos(\Delta\beta z)\right], \quad (5)$$

where $q_i(x,y) = E_i^x H_i^y - E_i^y H_i^x$ is an intensity factor, $q_{12}(x,y) = -E_2^y H_1^x + E_2^x H_1^y - E_1^y H_2^x + E_1^x H_2^y$ is a modal cross-overlap factor, and $\Delta\beta = \lambda/\Delta n_{\text{eff}}$ is due to Eigenmode dephasing, where $\Delta n_{\text{eff}} = n_{\text{eff},1} - n_{\text{eff},2}$. The fraction of power in the nanofluidic channel $p_1(z)$ is then given by

$$p_1(z) = \frac{\int_{A_{\text{bore}}} S_z(x,y,z)dA}{\int_{A_\infty} S_z(x,y,z)dA}, \quad (6)$$

where A_{bore} is the area of the central liquid-filled bore region. The results for the fraction of power $p_2(z)$ in the combined doped core and cladding region are obtained analogously, where we have verified that $p_2(z) = f_1 + f_2 - p_1(z)$. The results of the calculation are shown in Fig. 3(b) revealing a clear beating pattern and a periodic modulation of the power inside the liquid core region with the beat length L_B that is correlated to the difference in effective index by $L_B = \lambda/\Delta n_{\text{eff}}$. The emergence of a periodic beat pattern is a remarkable feature of the nanofluidic channel enhanced fiber given the fact that it operates in a non-phase-matched (i.e., off-resonance) configuration. This behavior is in stark contrast to commonly used directional mode couplers, requiring phase-matching to obtain a sufficient fringe contrast (e.g., [44]). Our calculations show distinctly different effective indices for the two relevant modes (HE_{11}: $n_{\text{eff},1} = 1.473556$, HE_{12}: $n_{\text{eff},2} = 1.460798$), leading to an effective index difference of $\Delta n_{\text{eff}} = 0.012758$ at $\lambda = 532$ nm resulting in a beat length of $L_B = 41.70$ μm. To compare with experiments, we fit our experimental data using,

$$P(z) = P_0 + \Delta P \cos\left[\frac{2\pi}{L_B}z + \phi_0\right]. \quad (7)$$

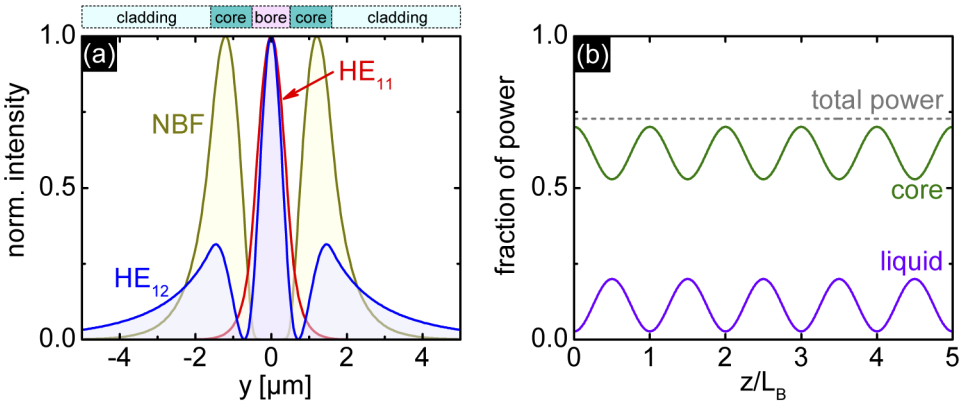

Fig. 3. (a) Intensity distribution of the three modes considered along an arbitrarily chosen line through the center of the fiber (red: HE_{11}, blue: HE_{12}, dark yellow: fundamental mode of the nanobore fiber). The top rectangles show the regions of liquid filled bore (light red), doped core (dark green) and cladding (light green). Each curve is normalized to its maximum value. (b) Fraction of power in liquid (purple) and core (green) as function of propagation distance calculated using Eq. (2), normalized to the beat length $L_B = 41.6$ μm.

Optical Materials EXPRESS

where P_0 is a power offset, and ΔP quantifies its maximum oscillation. Note that Eq. (7) has the same form as Eq. (5), with the addition of a phase offset ϕ_0 to account for the fact that the images were not taken at the beginning of the coupling section.

3. Experimental procedure

Figures 4(b) and (c) show two examples of recorded frames at two different points of time, both of which reveal a clear periodic oscillation of the fluorescent light along the direction of the fiber. To obtain the axial distribution of power $P_I(z)$ of the recorded fluorescence light per unit length as a function of the longitudinal position, the intensity $I(y, z)$ at a fixed z-position was transversely integrated within the liquid domain $P_I(z) = \int_{-\Delta y_0}^{\Delta y_0} I(y, z)dy$ (Δy_0: extension of liquid region). In this case the integration domain was considered as 7 pixels ($\Delta y_0 = 3$), referenced to the middle of the intensity pattern ($y = 0$ corresponds to the center of the nanochannel region). The resulting power distribution normalized to its maximum value $P_{\text{norm}}(z)$ is shown in Figs. 5(a) and (b), for the frames displayed in Figs. 4(b) and (c), respectively, and was fitted by Eq. (7) (dashed lines in Fig. 5) to obtain L_B. For both frames beat lengths of 42.42 μm and 41.30 μm were determined, which are close to the simulated value of 41.70 μm. This excellent agreement unambiguously confirms the modal interactions between the fundamental liquid HE_{11}- and the HE_{12}- modes, emerging as a result of the boundary between doped- and undoped- silica. The fitting parameters P_0, ΔP, and ϕ_0 are 0.437, −0.461, and 1.24, respectively for the pattern represented in Fig. 5(a), and 0.599, 0.365, and 1.34 for the pattern shown in Fig. 5(b). Note that photobleaching of the dye has not been observed and can entirely be ignored, since only the relative intensity of the interference pattern is relevant for the determination of the beat length. Additionally the laser was turned off during filling and only switched on once the liquid reached the domain of observation.

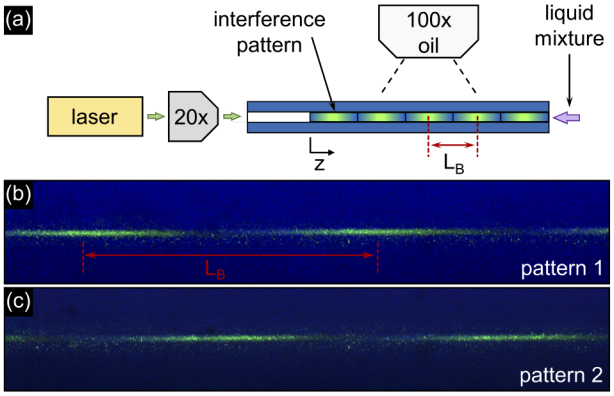

Fig. 4. (a) Schematic of the experimental setup to measure the beat length between the HE_{11} and the HE_{12}-modes. The modal interference creates an oscillating fluorescence pattern (examples of two frames are shown in (b) and (c)) that is collected perpendicularly to the fiber with a microscope objective.

The key feature that distinguishes our device from a typically directional mode coupler is that it operates in off-resonance (i.e., in non-phase-matched) mode while showing a substantial fringe contrast (Fig. 3(b)). This allows for wavelength independent refractive index sensing via the determination of the beat length $L_B = L_B(n_1)$, since the beat length which is directly correlated to the refractive index of the liquid n1is always determined at the same wavelength. Therefore this scheme can for instance be used to determine the thermo-optical coefficient of a particular liquid at one wavelength. Measuring a refractive index related quantity at a single wavelength is in

Optical Materials EXPRESS

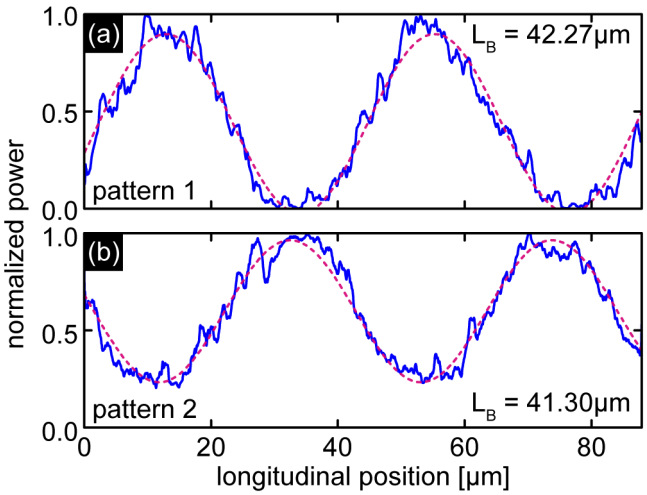

Fig. 5. Spatial distribution of the fluorescence power of the two patterns shown in 4(b) and (c) obtained by transversely integrating the intensity in the domain of the nano-channel (blue). The pink curves represent fits to the data points in order to determine the beat length L_B using Eq. 7.

contrast to the sensing principle of regular directional mode couplers which typically operate on-resonance, i.e., require phase-matching between the modes involved and therefore change the resonance wavelength in case the refractive index is modified [44].

To quantify the potential of the proposed wavelength-dependent refractive index sensing scheme from the simulation perspective, we have calculated the dependence of the effective

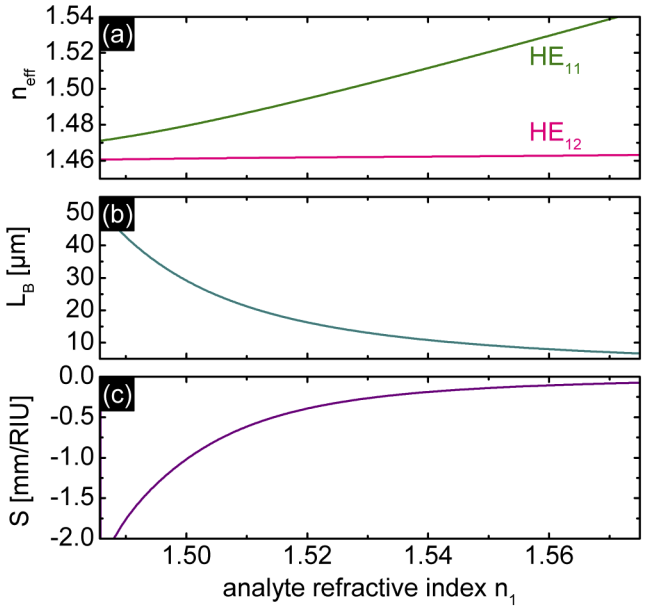

Fig. 6. (a) Dependence of the effective mode index of the two relevant modes (green: HE_{11}, pink: HE_{12}) as a function of analyte index n_1 (λ = 532 nm). (b) Corresponding beat length. (c) Resulting beat-length related refractive index sensitivity (slope of the curve shown in (b)) $S = dL_B(n_1)/dn_1$.

Optical Materials EXPRESS

mode index n_{eff} of the two relevant modes (green: HE_{11}, pink: HE_{12}) on analyte index n_1 and determine the corresponding beat length via $L_B = \lambda/n_{\text{eff}}$ and the beat-length related refractive index sensitivity $S = S(n_1)$ (Fig. 6).

The results show that particularly the effective index of the fundamental core mode (HE_{11}-mode) strongly increases in case the analyte index n_1 is increased (green curve in Fig. 6(a)), an effect that is much less pronounced for the HE_{12}-mode (pink curve in Fig. 6(b)). This different behavior results from the different relative concentrations of electromagnetic power of the two modes in the various materials (Fig. 6(c)) and in particular emphasizes the strong localization of the HE_{11} mode in the liquid analyte. The related beat length $L_B(n_1)$ therefore shows a strong dependence on the actual value of n_1 and thus a measurement of the beat length allows to directly determine the refractive index at the wavelength the measurement is performed. The beat-length related sensitivity $S = S(n_1)$ (Fig. 6(c)) can then be defined via the derivative of the beat length on refractive index $S = dL_B/dn_1$, reaching values of the order of 1 mm/RIU. Therefore, the proposed scheme can be employed in refractive index sensing applications using a single wavelength with off-the-shelf fiber components, requiring no additional equipment (e.g., spectrometer) besides the ability to observe the side-scattered light using a regular microscope. Note that other wavelengths can be chosen by using another dye.

4. Conclusions

The integration of novel materials into fiber allows to access unusual modal properties, offering new pathways for dispersion management, both of which allow to substantially increase the capabilities and application areas of optical fibers. We have presented a novel type of hybrid optical fiber that enables modal hybridization by including a high-index nanofluidic channel in the center of a doped silica core. The formation of higher-order modes with characteristic features that solely result from to the presence of two material interfaces is observed. The intensity and polarization patterns of the formed modes resemble those of higher-order modes in regular step-index fibers, with modal patterns that spatially overlap both with the nanofluidic channel and the doped core. In accordance with simulations, formation of hybridized modes was experimentally confirmed by directly measuring the beating (i.e,. the beat length) between the fundamental liquid HE_{11}-mode and one selected mode (here HE_{12}-mode) via side-wise detecting the periodically modulated fluorescence of the dye-doped nanofluidic channel. The excitation of such modes transfers 20% of the input to the nanofluidic channel, over a beat length of only 41.7 μm.

In order to compare our device to a commonly employed coupler design consisting of two parallel running waveguides, we have performed preliminary calculations comparing the presented device to an directional coupler formed by a 1 μm diameter nanochannel filled with the same liquid, in a silica cladding, adjacent and in contact with a doped core (index contrast: $8 \times 10{-}3$) of diameter 3.2 μm (λ = 532 nm). In the off-resonance (i.e., non-phase matching) case, the beat length is 93 μm (two times longer than the structure presented here), and the maximum power transfer that can be achieved is only 2%, which is ten times less compared to our device. Resonant directional coupling with 100% power transfer is achieved for an adjacent liquid channel diameter of 0.76 μm, reaching L_B = 230 μm. This suggests that the beat lengths of commonly used directional couplers are longer compared to our device as a result of the weak coupling that occurs solely via the evanescent tails.

A key difference to commonly employed couplers is that our multi-material hybrid fiber allows for the implementation of a directional coupler operating in off-resonance (i.e., in non-phase-matched) mode while still showing a substantial fringe contrast. This principally allows for wavelength independent refractive index sensing of liquid analytes (e.g. for investigating thermo-optic coefficients) as confirmed in simulations, representing a sensing scheme being in contrast to resonantly operating directional couplers typically employed.

Optical Materials EXPRESS

An alternate approach for coupling light to a liquid nanostrand using end-fire coupling [45], e.g., between a step-index fiber and a liquid-filled nano-capillary, is likely to result in comparable coupling efficiencies and no beating. However, such fiber/capillary interfaces are more challenging to produce, requiring multiple additional fabrication steps [35]. In contrast, producing the hybrid device presented here simply requires placing an off-the-shelf nanobore fiber in contact with a liquid. From the application perspective, the HE_{12} mode particularly interesting, since its polarization and intensity patterns in the nanofluidic channel correspond to those of the fundamental liquid (HE_{11}-) mode. This will likely benefit applications that demand strong coupling of the fundamental mode to a higher-order mode such as intermodal third-harmonic generation [36] or bidirectional coupling [43,46].

Funding. Alexander von Humboldt-Stiftung; Australian Research Council (DE200101041); Deutsche Forschungsgemeinschaft (SCHM2655/11-1, SCHM2655/12-1, SCHM2655/8-1); Fundação para a Ciência e a Tecnologia (SFRH/BD/129428/2017).

Acknowledgments. acknowledge support by the German Research Foundation and the Open Access Publication Fund of the Thueringer Universitaets- und Landesbibliothek Jena Projekt-Nr. 433052568 and Heraeus for fiber production.

Disclosures. The authors declare no conflicts of interest.

References

1. J. M. Dudley, G. Genty, and S. Coen, "Supercontinuum generation in photonic crystal fiber," Rev. Mod. Phys. **78**(4), 1135–1184 (2006).
2. I. Kaninow and T. Koch, *Optical Fiber Telecommunication IIIB* (Academic Press, 1997).
3. B. Lee, "Review of the present status of optical fiber sensors," Opt. Fiber Technol. **9**(2), 57–79 (2003).
4. Y. Z. Ma, Y. Sych, G. Onishchukov, S. Ramachandran, U. Peschel, B. Schmauss, and G. Leuchs, "Fiber-modes and fiber-anisotropy characterization using low-coherence interferometry," Appl. Phys. B **96**(2-3), 345–353 (2009).
5. S. Sakaguchi and S.-i. Todoroki, "Optical properties of GeO_2 glass and optical fibers," Appl. Opt. **36**(27), 6809 (1997).
6. Y. Ohmori, F. Hanawa, and M. Nakahara, "Fabrication of low-loss Al_2O_3-doped silica fibres," Electron. Lett. **18**(18), 761 (1982).
7. T. Katsuyama, T. Suganuma, K. Ishida, and G. Toda, "Refractive index behavior of SiO_2-P_2O_5 glass in optical fiber application," Opt. Commun. **21**(1), 182–184 (1977).
8. M. Cavillon, C. Kucera, T. W. Hawkins, N. Yu, P. Dragic, and J. Ballato, "Ytterbium-doped multicomponent fluorosilicate optical fibers with intrinsically low optical nonlinearities," Opt. Mater. Express **8**(4), 744 (2018).
9. M. A. Schmidt, A. Argyros, and F. Sorin, "Hybrid optical fibers – an innovative platform for in-fiber photonic devices," Adv. Opt. Mater. **4**(1), 13–36 (2016).
10. J. Hou, D. Bird, A. George, S. Maier, B. T. Kuhlmey, and J. C. Knight, "Metallic mode confinement in microstructured fibres," Opt. Express **16**(9), 5983–5990 (2008).
11. P. Uebel, M. A. Schmidt, H. W. Lee, and P. S. Russell, "Polarisation-resolved near-field mapping of a coupled gold nanowire array," Opt. Express **20**(27), 28409–28417 (2012).
12. H. K. Tyagi, M. A. Schmidt, L. P. Sempere, and P. S. Russell, "Optical properties of photonic crystal fiber with integral micron-sized Ge wire," Opt. Express **16**(22), 17227–17236 (2008).
13. P. J. A. Sazio, A. Amezcua-Correa, C. E. Finlayson, J. R. Hayes, T. J. Scheidemantel, N. F. Baril, B. R. Jackson, D. J. Won, F. Zhang, E. R. Margine, V. Gopalan, V. H. Crespi, and J. V. Badding, "Microstructured optical fibers as high-pressure microfluidic reactors," Science **311**(5767), 1583–1586 (2006).
14. M. Bayindir, F. Sorin, A. F. Abouraddy, J. Viens, S. D. Hart, J. D. Joannopoulos, and Y. Fink, "Metal-insulator-semiconductor optoelectronic fibres," Nature **431**(7010), 826–829 (2004).
15. E. Bormashenko, R. Pogreb, and S. Sutovski, *Optical properties of polymer/chalcogenide glass composite materials*, vol. 4097 *of International Symposium on Optical Science and Technology* (SPIE, 2000).
16. N. Granzow, M. A. Schmidt, W. Chang, L. Wang, Q. Coulombier, J. Troles, P. Toupin, I. Hartl, K. F. Lee, M. E. Fermann, L. Wondraczek, and P. S. Russell, "Mid-infrared supercontinuum generation in As_2S_3-silica "nano-spike" step-index waveguide," Opt. Express **21**(9), 10969–10977 (2013).
17. A. Tuniz, M. Chemnitz, J. Dellith, S. Weidlich, and M. A. Schmidt, "Hybrid-mode-assisted long-distance excitation of short-range surface plasmons in a nanotip-enhanced step-index fiber," Nano Lett. **17**(2), 631–637 (2017).
18. R. R. He, P. J. A. Sazio, A. C. Peacock, N. Healy, J. R. Sparks, M. Krishnamurthi, V. Gopalan, and J. V. Badding, "Integration of gigahertz-bandwidth semiconductor devices inside microstructured optical fibres," Nat. Photonics **6**(3), 174–179 (2012).
19. S. R. Xie, F. Tani, J. C. Travers, P. Uebel, C. Caillaud, J. Troles, M. A. Schmidt, and P. S. J. Russell, "As_2S_3-silica double-nanospike waveguide for mid-infrared supercontinuum generation," Opt. Lett. **39**(17), 5216–5219 (2014).

Optical Materials EXPRESS

20. L. Shen, N. Healy, L. Xu, H. Y. Cheng, T. D. Day, J. H. V. Price, J. V. Badding, and A. C. Peacock, "Four-wave mixing and octave-spanning supercontinuum generation in a small core hydrogenated amorphous silicon fiber pumped in the mid-infrared," Opt. Lett. **39**(19), 5721–5724 (2014).
21. S. Pumpe, M. Chemnitz, J. Kobelke, and M. A. Schmidt, "Monolithic optofluidic mode coupler for broadband thermo- and piezo-optical characterization of liquids," Opt. Express **25**(19), 22932 (2017).
22. T. Euser, M. Garbos, J. Chen, and P. S. J. Russell, "Precise balancing of viscous and radiation forces on a particle in liquid-filled photonic bandgap fiber," Opt. Lett. **34**(23), 3674–3676 (2009).
23. S. Jiang, J. Zhao, R. Förster, S. Weidlich, M. Plidschun, J. Kobelke, R. Fatobene Ando, and M. A. Schmidt, "Three dimensional spatiotemporal nano-scale position retrieval of the confined diffusion of nano-objects inside optofluidic microstructured fibers," Nanoscale **12**(5), 3146–3156 (2020).
24. R. Förster, S. Weidlich, M. Nissen, T. Wieduwilt, J. Kobelke, A. M. Goldfain, T. K. Chiang, R. F. Garmann, V. N. Manoharan, Y. Lahini, and M. A. Schmidt, "Tracking and analyzing the Brownian motion of nano-objects inside hollow core fibers," ACS Sens. **5**(3), 879–886 (2020).
25. D. K. C. Wu, B. T. Kuhlmey, and B. J. Eggleton, "Ultrasensitive photonic crystal fiber refractive index sensor," Opt. Lett. **34**(3), 322–324 (2009).
26. Z. He, F. Tian, Y. Zhu, N. Lavlinskaia, and H. Du, "Long-period gratings in photonic crystal fiber as an optofluidic label-free biosensor," Biosens. Bioelectron. **26**(12), 4774–4778 (2011).
27. L. Yuan, J. Huang, X. Lan, H. Wang, L. Jiang, and H. Xiao, "All-in-fiber optofluidic sensor fabricated by femtosecond laser assisted chemical etching," Opt. Lett. **39**(8), 2358–2361 (2014).
28. S. Ertman, P. Lesiak, and T. R. Woliński, "Optofluidic photonic crystal fiber-based sensors," J. Lightwave Technol. **35**(16), 3399–3405 (2017).
29. L. Liang, C. Zhao, F. Xie, L.-P. Sun, Y. Ran, L. Jin, and B.-O. Guan, "Sensitivity enhancement of a fiber-based interferometric optofluidic sensor," Opt. Express **28**(17), 24408 (2020).
30. P. Vaiano, B. Carotenuto, M. Pisco, A. Ricciardi, G. Quero, M. Consales, A. Crescitelli, E. Esposito, and A. Cusano, "Lab on fiber technology for biological sensing applications," Laser Photonics Rev. **10**(6), 922–961 (2016).
31. J. S. Chen, T. G. Euser, N. J. Farrer, P. J. Sadler, M. Scharrer, and P. S. J. Russell, "Photochemistry in photonic crystal fiber nanoreactors," Chem. Eur. J. **16**(19), 5607–5612 (2010).
32. A. M. Cubillas, M. Schmidt, M. Scharrer, T. G. Euser, B. J. Etzold, N. Taccardi, P. Wasserscheid, and P. S. J. Russell, "Ultra-low concentration monitoring of catalytic reactions in photonic crystal fiber," Chem. Eur. J. **18**(6), 1586–1590 (2012).
33. M. Vieweg, T. Gissibl, S. Pricking, B. T. Kuhlmey, D. C. Wu, B. J. Eggleton, and H. Giessen, "Ultrafast nonlinear optofluidics in selectively liquid-filled photonic crystal fibers," Opt. Express **18**(24), 25232–25240 (2010).
34. G. Fanjoux, A. Sudirman, J.-C. Beugnot, L. Furfaro, W. Margulis, and T. Sylvestre, "Stimulated Raman–Kerr scattering in an integrated nonlinear optofluidic fiber arrangement," Opt. Lett. **39**(18), 5407–5410 (2014).
35. S. Kedenburg, T. Gissibl, T. Steinle, A. Steinmann, and H. Giessen, "Towards integration of a liquid-filled fiber capillary for supercontinuum generation in the 1.2–2.4 μm range," Opt. Express **23**(7), 8281–8289 (2015).
36. K. Schaarschmidt, H. Xuan, J. Kobelke, M. Chemnitz, I. Hartl, and M. A. Schmidt, "Long-term stable supercontinuum generation and watt-level transmission in liquid-core optical fibers," Opt. Lett. **44**(9), 2236–2239 (2019).
37. A. Sharafali and K. Nithyanandan, "A theoretical study on the supercontinuum generation in a novel suspended liquid core photonic crystal fiber," Appl. Phys. B **126**(4), 55 (2020).
38. D. Lopez-Cortes, O. Tarasenko, and W. Margulis, "All-fiber Kerr cell," Opt. Lett. **37**(15), 3288–3290 (2012).
39. R. M. Gerosa, A. Sudirman, L. d. S. Menezes, W. Margulis, and C. J. de Matos, "All-fiber high repetition rate microfluidic dye laser," Optica **2**(2), 186–193 (2015).
40. M. Chemnitz, M. Gebhardt, C. Gaida, F. Stutzki, J. Kobelke, J. Limpert, A. Tünnermann, and M. A. Schmidt, "Hybrid soliton dynamics in liquid-core fibres," Nat. Commun. **8**(1), 42 (2017).
41. I. H. Malitson, "Interspecimen comparison of the refractive index of fused silica," J. Opt. Soc. Am. **55**(10), 1205–1209 (1965).
42. J. A. Snyder and J. D. Love, *Optical Waveguide Theory* (Chapman and Hall, 1983).
43. A. Tuniz and M. A. Schmidt, "Broadband efficient directional coupling to short-range plasmons: towards hybrid fiber nanotips," Opt. Express **24**(7), 7507–7524 (2016).
44. H. W. Lee, M. A. Schmidt, P. Uebel, H. Tyagi, N. Y. Joly, M. Scharrer, and P. S. Russell, "Optofluidic refractive-index sensor in step-index fiber with parallel hollow micro-channel," Opt. Express **19**(9), 8200–8207 (2011).
45. R. G. Hunsperger, A. Yariv, and A. Lee, "Parallel end-butt coupling for optical integrated circuits," Appl. Opt. **16**(4), 1026–1032 (1977).
46. A. Tuniz, T. Wieduwilt, and M. A. Schmidt, "Tuning the effective PT phase of plasmonic eigenmodes," Phys. Rev. Lett. **123**(21), 213903 (2019).